OpenIllumination: A Multi-Illumination Dataset for Inverse Rendering Evaluation on Real Objects

Isabella Liu[1*], Linghao Chen[1,2*], Ziyang Fu[1], Liwen Wu[1], Haian Jin[2], Zhong Li[3],

Chin Ming Ryan Wong[3], Yi Xu[3], Ravi Ramamoorthi[1], Zexiang Xu[4], Hao Su[1]

[1]UC San Diego, [2]Zhejiang University, [3] OPPO US Research Center,
[4] Adobe Research, *Equal Contribution,
{lal005,zifu,liw026,ravi,haosu}@ucsd.edu
{chenlinghao,haian}@zju.edu.cn
zexiangxu@gmail.com
{zhong.li,ryan.wong,yi.xu}@oppo.com

Abstract

We introduce OpenIllumination, a real-world dataset containing over 108K images of 64 objects with diverse materials, captured under 72 camera views and a large number of different illuminations. For each image in the dataset, we provide accurate camera parameters, illumination ground truth, and foreground segmentation masks. Our dataset enables the quantitative evaluation of most inverse rendering and material decomposition methods for real objects. We examine several state-of-the-art inverse rendering methods on our dataset and compare their performances. The dataset and code can be found on the project page: https://oppo-us-research.github.io/OpenIllumination.

1 Introduction

Recovering object geometry, material, and lighting from images is a crucial task for various applications, such as image relighting and view synthesis. While recent works have shown promising results by using a differentiable renderer to optimize these parameters using the photometric loss [52, 54, 53, 20, 33], they can only perform a quantitative evaluation on synthetic datasets since it is easy to obtain ground-truth information. In contrast, they can only show qualitative results instead of providing quantitative evaluations in real scenes.

Nevertheless, it is crucial to acknowledge the inherent gap between synthetic and real-world data, for real-world scenes exhibit intricate complexities, such as natural illuminations, diverse materials, and complex geometry, which may present challenges that synthetic data fails to model accurately. Consequently, it becomes imperative to complement synthetic evaluation with real-world data to validate and assess the ability of inverse rendering algorithms in practical settings.

It is highly challenging to capture real objects in practice. A common approach to capturing real-world data is using a handheld camera [20, 54]. Unfortunately, this approach frequently introduces the occlusion of ambient light by photographers and cameras, consequently resulting in different illuminations for each photograph. Such discrepancies are unreasonable for most methods that assume a single constant illumination. Furthermore, capturing images under multiple illuminations with a handheld camera often produces images with highly different appearances and results in inaccurate and even fail camera pose estimation, particularly for feature matching-based methods such as COLMAP [38]. Recent efforts have introduced some datasets [34, 44, 21] that incorporate
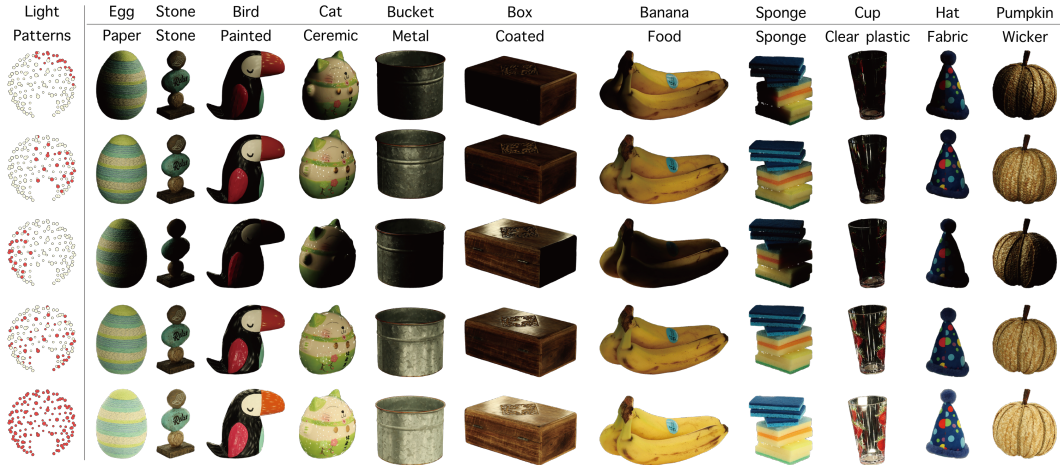
Figure 1: **Some example images in the proposed dataset.** The dataset contains images of various objects with diverse materials, captured under different views and illuminations. The leftmost column visualizes several different illumination patterns, with **red** and yellow indicating activated and deactivated lights. The name and material for each object are listed in the first and second rows. The materials are selected from the OpenSurfaces [3] dataset.

multiple illuminations in real-world settings. However, as shown in Tab. 1, most of them are limited either in the number of views [34, 21] or the number of illuminations [21]; few of them provide object-level data as well. Consequently, these existing datasets prove unsuitable for evaluating inverse rendering methods on real-world objects.

To address this, we present a new dataset containing objects with a variety of materials, captured under multiple views and illuminations, allowing for reliable evaluation of various inverse rendering tasks with real data. Our dataset was acquired using a setup similar to a traditional light stage [10, 11], where densely distributed cameras and controllable lights are attached to a static frame around a central platform. In contrast to handheld capture, this setup allows us to precisely pre-calibrate all cameras with carefully designed calibration patterns and reuse the same camera parameters for all the target objects, leading to not only high calibration accuracy but also a consistent evaluation process (with the same camera parameters) for all the scenes.

On the other hand, the equipped multiple controllable lights enable us to flexibly illuminate objects with a large number of complex lighting patterns, facilitating the acquisition of illumination ground truth.

Dataset	Capturing device	Lighting condition	Number of illuminations	HDR	Number of scenes/objects	Number of views
DTU [19]	gantry	pattern	7	✗	80 scenes	49/64
NeRF-OSR [37]	commodity camera	env	5∼11	✗	9 scenes	∼360
DiLiGenT [40]	commodity camera	OLAT	96	✓	10 objects	1
DiLiGenT-MV [27]	studio/desktop scanner	OLAT	96	✓	5 objects	20
NeROIC [23]	commodity camera	env	4∼6	✗	3 objects	40
MIT-Intrinsic [15]	commodity camera	OLAT	10	✗	20 objects	1
Murmann et al. [34]	light probe	env	25	✗	1000 scenes	1
LSMI [21]	light probe	env	3	✗	2700 scenes	1
ReNe [44]	gantry	OLAT	40	✗	20 objects	50
Ours	light stage	pattern+OLAT	13 pattern+ 142 OLAT	✓	64 objects	72

Table 1: **Comparison between representative multi-illumination real-world datasets.** Env. stands for environment lights.

With the help of high-speed cameras running at 30 fps, we are able to capture OLAT (One-Light-At-a-Time) images with a very high efficiency, which is critical for capturing data at a large scale. In the end, we have captured over 108K images, each with a well-calibrated camera and illumination

parameters. Moreover, we also provide high-quality object segmentation masks by designing an efficient semi-automatic mask labeling method.

We conduct baseline experiments on several tasks: (1) joint geometry-material-illumination estimation; (2) joint geometry-material estimation under known illumination; (3) photometric stereo reconstruction; (4) Novel view synthesis to showcase the ability to evaluate real objects on our dataset. To the best of our knowledge, by the time of this paper's submission, there are no other real datasets that can be used to perform the quantitative evaluation for relighting on real data.

In summary, our contributions are as follows:

- We capture over 108K images for real objects with diverse materials under multiple viewpoints and illuminations, which enables a more comprehensive analysis for inverse rendering tasks across various material types.

- The proposed dataset provides precise camera calibrations, lighting ground truth and accurate object segmentation masks.

- We evaluate and compare the performance of multiple state-of-the-art (SOTA) inverse rendering and novel view synthesis methods. We perform quantitive evaluation of relighting real object under unseen illuminations.

2   Related works

Inverse rendering.   Inverse rendering has been a long-standing task in the fields of computer vision and graphics, which focuses on reconstructing shapes and materials from multi-view 2D images. A great amount of work [5, 14, 18, 26, 48, 35, 53, 55] has been proposed for this task. Some of them make use of learned domain-specific priors [5, 12, 2, 28]. Some other works rely on controllable capture settings to estimate the geometry and material, such as structure light [49], circular LED lights [56], collocated camera and flashlight [51, 5, 4], and so on.

Recently, a lot of works use neural representations to support inverse rendering reconstruction under unknown natural lighting conditions [20, 6, 53, 55, 7, 33, 52]. By combining the popular neural representations such as NeRF [31] or SDF [46, 50] with physically-based rendering model [8], they can achieve shape and reflectance reconstruction with image loss constraint. Although these works can achieve high-quality reconstruction, they can only evaluate relighting performance under novel illumination on synthetic data because of the lack of high-quality real object datasets.

Multi-illumination datasets.   Multi-illumination observations intuitively provide more cues for computer vision and graphics tasks like inverse rendering. Some works have utilized the temporal variation of natural illumination, such as sunlight and outdoor lighting. These "in-the-wild" images are typically captured using web cameras [47, 42, 37, 24] or using controlled camera setups [41, 25]. Another line of work focuses on indoor scenes, while indoor scenes generally lack a readily available source of illumination that exhibits significant variation. In this case, a common approach involves using flash and no-flash pairs [36, 13, 1]. Applications like denoising, mixed-lighting white balance, and BRDF capture benefits from these kinds of datasets. However, other applications like photometric stereo and inverse rendering usually require more than two images and more lighting conditions for reliable results, which these datasets often fail to provide.

3   Dataset construction

3.1   Dataset overview

The OpenIllumination dataset contains over 108K images of 64 objects with diverse materials. Each object is captured by 48 DSLR cameras under 13 lighting patterns. Additionally, 20 objects are captured by 24 high-speed cameras under 142 OLAT setting.

Fig. 1 shows some images captured under different lighting patterns, while the images captured under OLAT illumination can be found in Fig. 5.
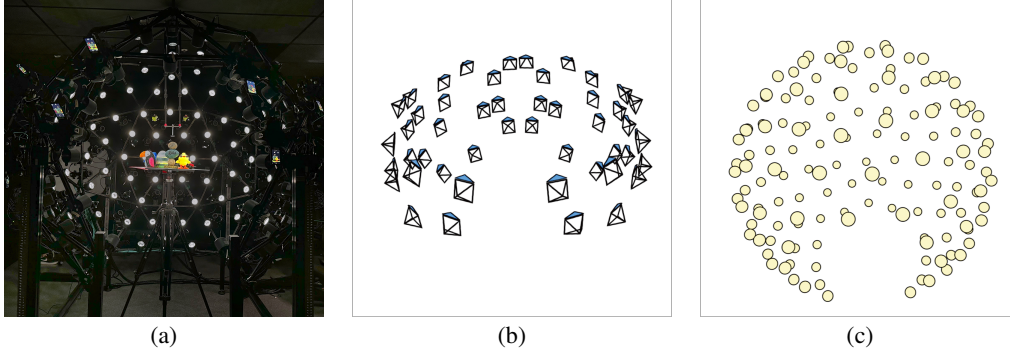
(a)   (b)   (c)

Figure 2: (a) The capturing system contains 48 DSLR cameras (Canon EOS Rebel SL3), 24 high-speed cameras (HR-12000SC), and 142 controllable linear polarized LED. (b) The calibrated DSLR camera poses. (c) The reconstructed light positions.

Our dataset includes a total of 24 diverse material categories, such as plastic, glass, fabric, ceramic, and more. Note that one object may possess several different materials, thus the number of materials is larger than the number of objects.

3.2 Camera calibration

The accuracy of camera calibration highly affects the performance of most novel view synthesis and inverse rendering methods. Previous works [20, 54] typically capture images by handheld cameras and employ COLMAP [38] to estimate camera parameters. However, this approach heavily relies on the object's textural properties, which is challenging in instances where the object lacks texture or exhibits specular reflections from certain viewpoints. These challenges can obstruct accurate feature matching, consequently reducing the precision of camera parameter estimation. Ultimately, the reliability of inverse rendering outcomes is undermined, and finding out whether inaccuracies are caused by erroneous camera parameters or limitations of the inverse rendering method itself becomes a challenging problem. Leveraging the capabilities of our light stage, wherein camera intrinsics and extrinsic can be fixed when capturing different objects, we employ COLMAP to recover the camera parameters on a rich textured and low-specularity scene. For each subsequently captured object, we use this set of camera parameters instead of performing recalibration. The results of camera calibration are visualized in Fig. 2(b).
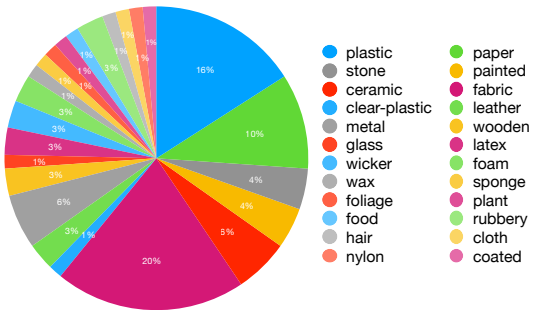
3.3 Light calibration

In this section, we propose a chrome-ball-based lighting calibration method to obtain the ground-truth illumination which plays a critical role in the relighting evaluation.

Our data are captured in a dark room where a set of linear polarized LEDs are placed on a sphere uniformly as the only lighting source. Each light can be approximated by a Spherical Gaussian (SG), defined as the following form [45]:

$$G(\nu; \boldsymbol{\xi}, \lambda, \boldsymbol{\mu}) = \boldsymbol{\mu}\, e^{\lambda(\nu \cdot \boldsymbol{\xi} - 1)}, \tag{1}$$

where $\nu \in \mathbb{S}^2$ is the function input, representing the incident lighting direction to query, $\boldsymbol{\xi} \in \mathbb{S}^2$ is the lobe axis, $\lambda \in \mathbb{R}_+$ is the lobe sharpness, and $\boldsymbol{\mu} \in \mathbb{R}_+^n$ is the lobe amplitude.

We utilize a chrome ball to estimate the 3D position of each light. Assuming the chrome ball is highly specular and isotropic, its position and radius are known, and cameras and lights are evenly distributed around the chrome ball. For each LED single light, at least one camera can capture the reflected light rays out from its starting location. The incident light direction can be computed via:

$$I = -T + 2(I \cdot N)N, \tag{2}$$

4

where I is the incident light direction that goes out from the point of incidence, N is the normal of the intersection point on the surface, and T is the direction of the reflected light.

For each LED light, its point of incidence on the chrome ball can be captured by multiple cameras, and for each camera i, we can compute an incident light direction I_i, which should have the least distance from the LED light location p. Therefore, to leverage information from multiple camera viewpoints, we seek to minimize the sum of distances between the light position and incident light directions across different camera views. This optimization is expressed as:

$$L(p) = \sum_i d(p, I_i), \|p\| = 1, \qquad (3)$$
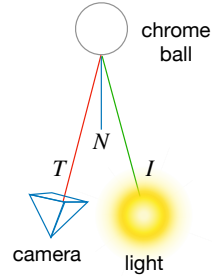
where p represents the light position to be determined, $d(p, I_i)$ denotes the L2 distance between the light and the incident light direction corresponding to view i, and the constraint $\|p\| = 1$ ensures that the lights lie on the same spherical surface as the cameras. The reconstructed light distribution, depicted in Fig. 2(c), closely aligns with the real-world distribution.

After estimating the 3D position for each light, we need to determine the lobe size for them. Since the lights in our setup are of the same type, we can estimate a global lobe size for all lights. By taking one OLAT image of the chrome ball as input, we flatten it into an environment map. Subsequently, we optimize the parameters of the Spherical Gaussians (SGs) model to minimize the difference between the computed environment map and the observed environment map. The final fitted lobe size parameter we use is 236.9705. Since all the lights have identical lighting intensities, and the lighting intensity can be of arbitrary scale because of the scale ambiguity between the material and lighting, we set the lighting intensity to 5 for all lights.

3.4 Semi-automatic high-quality mask labeling

To obtain high-quality segmentation masks, we use Segment-Anything [22] (SAM) to perform instance segmentation. However, we find that the performance is not satisfactory. One reason is that the object categories are highly undefined. In this case, even combining the bounding box and point prompts cannot produce satisfactory results. To address this problem, we use multiple bounding-box prompts to perform segmentation for each possible part and then calculate a union of the masks as the final object mask. For objects with very detailed and thin structures, e.g. hair, we use an off-the-shelf background matting method [29] to perform object segmentation.

4 Baseline experiments

4.1 Inverse rendering evaluation

In this section, we conduct experiments employing various learning-based inverse rendering methods on our dataset. Throughout these experiments, we carefully select 10 objects exhibiting a diverse range of materials, and we partition the images captured by DSLR cameras into training and testing sets, containing 38 and 10 views respectively.

Baselines. We validate six recent learning-based inverse rendering approaches assuming single illumination conditions: NeRD [6], Neural-PIL [7], PhySG [52], InvRender [55], nvdiffrec-mc [16], and TensoIR [20]. Moreover, we validate three of them [6, 7, 20] that support multiple illumination optimization.

Joint geometry-material-illumination estimation. For experiments under single illumination, we use images captured with all lights activated, while for multi-illumination, we select images taken under three different lighting patterns.

NeRD[6] is observed to exhibit high instability. In many cases, NeRD fails to learn a meaningful environment map. Neural-PIL [7] generates fine environment maps and produces high-quality renderings. However, the generated environment map incorporates the albedo of objects and fails to produce reasonable diffuse results in multi-illumination conditions. Both NeRD and Neural-PIL suffer from map fractures in roughness, normal, and albedo, providing visible circular cracks, which we attribute to the overfitting of the environment map, where certain colors become embedded
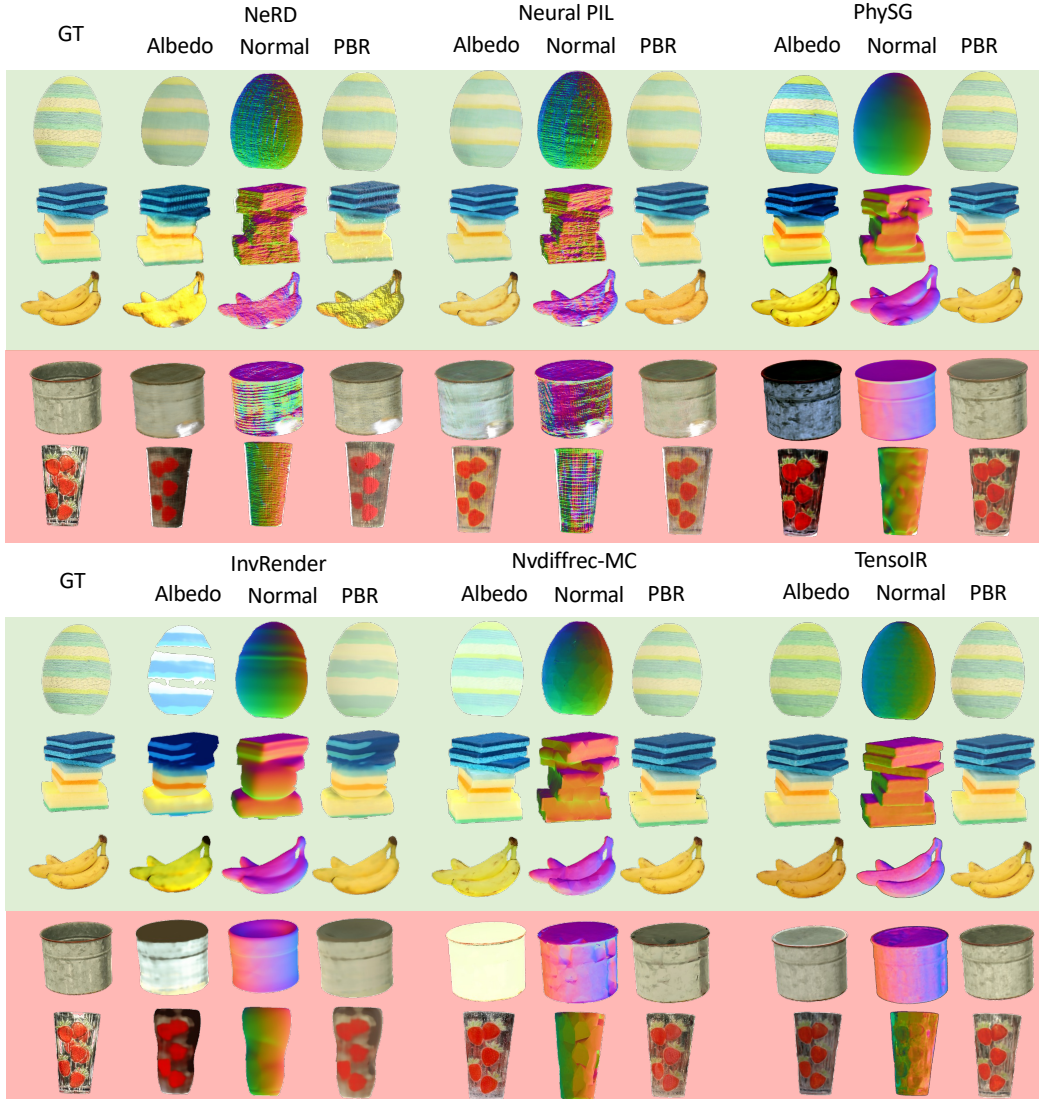
Figure 3: The object reconstruction on our dataset from three inverse rendering baselines under single illumination. Objects highlighted by **green** color are easier tasks in our dataset, while objects in **red** color are more difficult tasks that involve more complicated materials like metal and clear plastic.

within it. PhySG [52] applies specular BRDFs allowing for a better approximate evaluation of light transport. PhySG shows commendable results on metal and coated materials, simulating a few highlights. However its geometry learning was inaccurate, and it performed poorly in objects with multiple specular parts, failing to reproduce any prominent highlights. InvRender [55] models spacially-varying indirection illumination and the visibility of direct illumination. However, its reconstructed geometry tends to lack detail and be over-smooth on some objects. nvdiffrec-mc [16] incorporates Monte Carlo integration and a denoising module during rendering to achieve a more efficient and stable convergence in optimization. It achieves satisfactory relighting results on most objects. But the quality of geometry detail as shown in the reconstructed normal map is affected by the grid resolution of DMTet [39]. TensoIR [20] also exhibits satisfactory performance. However, it still encounters challenges in generating good results for highly specular surfaces, as shown in the fourth row in Fig. 3. Moreover, since TensoIR models materials using a simplified version of Disney BRDF [8], which fixes the F_0 in the fresnel term to be 0.04, its representation capabilities are limited, and certain materials such as metal and transparent plastic may not be accurately modeled, as illustrated in the fifth row in Fig. 3 and Tab. 2, where TensoIR only achieve about 22 PSNR on the translucent plastic cup.

Overall, all the methods struggle with modeling transparency or complex reflectance because of the relatively simple BRDF used in rendering. For concave objects, such as the metal bucket shown in Fig. 3, NeRF-based methods have difficulty learning the correct geometry. In addition, compared to single illumination, two of our baselines, NeRD and NeuralPIL show inferior performance under multi-illumination, and the baseline TensoIR maintains a high quality of the reconstruction.

Object	egg	stone	bird	box	pumpkin	hat	cup	sponge	banana	bucket
Material	paper	stone	painted	coated	wooden	fabric	clear plastic	sponge	food	metal
NeRD	33.40	27.20	26.81	22.80	23.81	27.64	22.06	26.78	25.54	26.14
Neural-PIL	34.42	29.41	29.17	25.49	27.59	30.14	22.55	31.01	31.61	27.73
PhySG	35.06	30.72	29.02	26.56	27.32	31.16	21.86	30.70	34.39	29.25
InvRender	31.52	25.51	24.96	23.80	25.43	22.79	21.62	24.20	29.34	26.18
nvdiffrec-mc	35.77	31.51	30.20	27.29	28.12	31.19	22.08	32.68	35.60	28.52
TensoIR	34.88	29.96	30.21	26.80	28.20	31.96	22.13	32.49	34.77	29.32

Table 2: **Inverse rendering evaluation results under single illumination.** We validate six inverse rendering baselines with static illumination. We report the PSNR results for each object.

Object	egg	stone	bird	box	pumpkin	hat	cup	sponge	banana	bucket
Material	paper	stone	painted	coated	wooden	fabric	clear plastic	sponge	food	metal
NeRD	26.32	24.20	24.34	21.05	18.74	23.14	21.59	17.73	21.22	16.48
Neural-PIL	30.84	28.48	28.47	25.45	25.74	29.80	**22.44**	29.41	30.59	26.06
TensoIR	**34.51**	**29.88**	**30.21**	**26.53**	**27.96**	**31.58**	22.09	**31.87**	**34.35**	**28.91**

Table 3: **Inverse rendering evaluation results under multi-illumination.** We select three light patterns from our dataset to validate three baselines that support multiple illuminations. We report the PSNR results for each object.
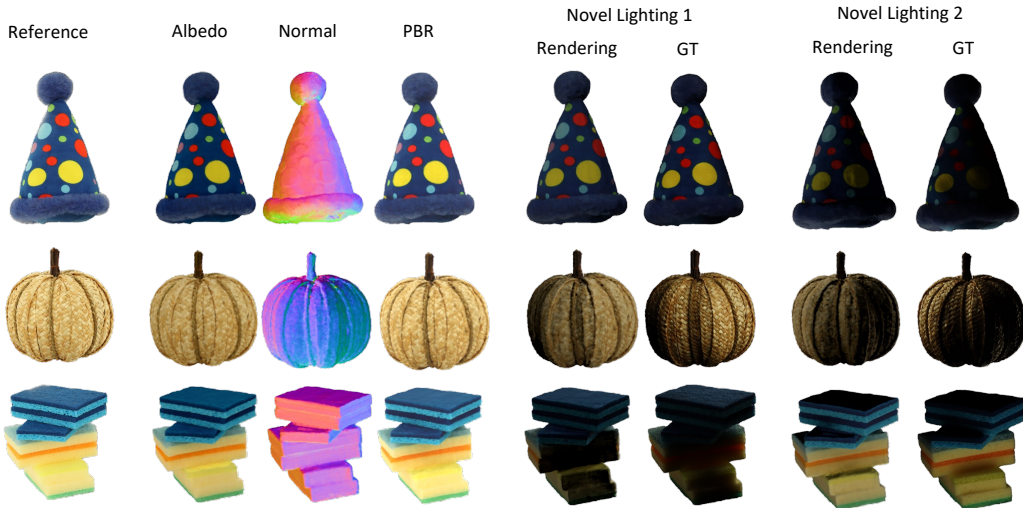
Figure 4: Relighting results of TensoIR under novel illumination. We show the reconstructed albedo, normal, and PBR results. For each novel illumination, we show the rendering and ground-truth captured images.

Joint geometry-material estimation under known illumination. As introduced in Sec. 3.1, we capture the objects under different illuminations. For each illumination, we provide illumination ground truth represented as a combination of Spherical Gaussian functions. This enables us to evaluate the performance of relighting under novel illumination with the decomposed material and geometry.

Object	egg	stone	bird	box	pumpkin	hat	cup	sponge	banana	bucket
Material	paper	stone	painted	coated	wooden	fabric	clear plastic	sponge	food	metal
PSNR	31.99	31.07	30.16	27.57	27.16	32.38	22.96	30.86	32.13	27.13

Table 4: Performance of relighting under novel illumination using TensoIR.

Tab. 4 shows the relighting performance of TensoIR [20] on 10 objects. Fig. 4 shows the material decomposition and the relighting visualizations. In general, TensoIR performs better on diffuse objects than on metal and transparent objects.

4.2 Photometric stereo

Photometric stereo (PS) is a well-established technique to reconstruct a 3D surface of an object [18]. The method estimates the shape and recovers surface normals of a scene by utilizing several intensity images obtained under varying illumination conditions with an identical viewpoint [17, 43]. By default, PS assumes a Lambertian surface reflectance, in which normal vectors and image intensities are linearly dependent on each other. During our capturing, we place circular polarizers over each light source, we also place a circular polarizer of the same sense in front of the camera to cancel out the specular reflections [30]. Fig. 5 shows the reconstructed albedo and normal map from the OLAT images in our dataset.
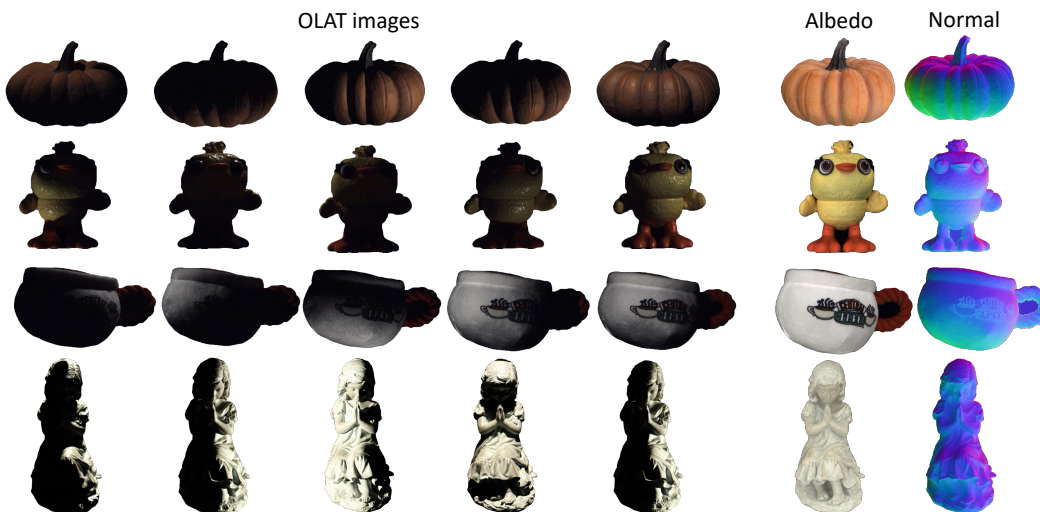
Figure 5: Results of photometric stereo using the OLAT images in our dataset.

4.3 Novel view synthesis

Object	egg	stone	bird	box	pumpkin	hat	cup	sponge	banana	bucket
Material	paper	stone	painted	coated	wooden	fabric	clear plastic	sponge	food	metal
NeRF [31]	33.53	29.32	29.64	25.38	26.95	31.29	**22.52**	31.36	33.65	28.54
TensoRF [9]	32.42	29.84	28.45	**25.49**	27.54	31.50	20.87	31.34	34.32	29.28
I-NGP [32]	**34.07**	**30.62**	29.91	25.83	**27.93**	**32.51**	22.51	**32.71**	**34.98**	29.72
NeuS [46]	33.43	29.78	**30.00**	25.47	27.83	31.93	22.13	32.44	34.17	**29.99**

Table 5: **Novel-view-synthesis PSNR on NeRF, TensoRF, Instant-NGP, and NeuS.**

While our dataset was primarily proposed for evaluating inverse rendering approaches, the multi-view images in it can also serve as a valuable resource for evaluating novel view synthesis methods. In

this section, we perform experiments utilizing several neural radiance field methods to validate the data quality of our dataset. We conduct experiments employing the vanilla NeRF [31], TensoRF [9], Instant-NGP [32], and NeuS [46]. The quantitative results, as presented in Tab. 5, demonstrate the exceptional quality of our data and the precise camera calibration, as evidenced by the consistently high PSNR scores attained.

4.4 Ablation study

Inconsistency between views   Hand-held camera reconstruction   Our dataset reconstruction

(a)   **(b)**
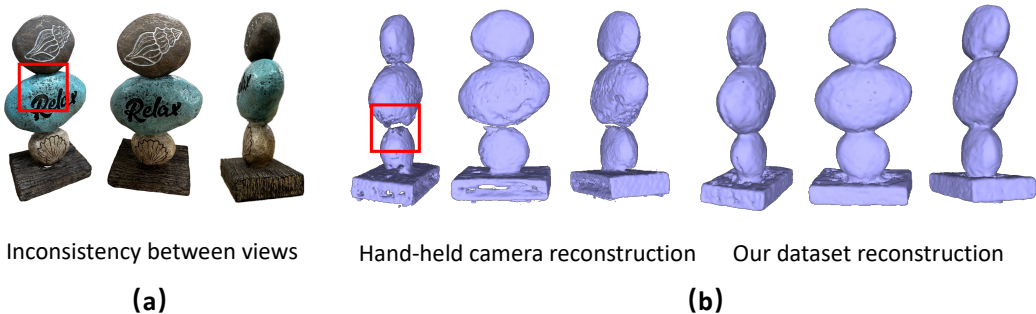
Figure 6: **(a)** Capturing using a handheld camera often introduces inconsistent illuminations. **(b)** Geometry reconstruction using data in our dataset delivers higher completion than using data captured by handheld cameras.

As depicted in Fig. 6 (a), the utilization of handheld cameras in the capture process frequently gives rise to inconsistent illumination between different viewpoints because of the changing occlusion of light caused by the moving photographer, thereby breaching the static illumination assumption for most inverse rendering methods. In Fig. 6 (b), we use a handheld smartphone to capture data under a similar setup in the dome. Experiments on handheld cameras tends to inadequately ensure an extensive range of viewpoints, thereby frequently resulting in the incompleteness of the reconstructed objects. Conversely, our dataset delivers a superior range of viewpoints and maintains consistency across different objects, thereby producing a more complete reconstruction. This demonstrates the high quality of our dataset and establishes its suitability as an evaluation benchmark for real-world objects.

5 Limitation

There are several limitations and future directions to our work. **(1)** Since we use the light stage to capture the images in a dark room, the illumination is controlled strictly. Thus there exists a gap between the images in this dataset and in-the-wild captured images. **(2)** Although we use state-of-the-art methods for segmentation, the mask consistency across different views for smaller objects with fine details, such as hair, is not considered yet. **(3)** Due to the limited space, the sizes of the objects in the dataset are restricted to 10∼20 cm, and the cameras are not highly densely distributed.

6 Conclusion

In this paper, we introduce a multi-illumination dataset OpenIllumination for inverse rendering evaluation on real objects. This dataset offers crucial components such as precise camera parameters, ground-truth illumination information, and segmentation masks for all the images. OpenIllumination provides a valuable resource for quantitatively evaluating inverse rendering and material decomposition techniques applied to real objects for researchers. By analyzing various state-of-the-art inverse rendering pipelines using our dataset, we have been able to assess and compare their performance effectively. The release of both the dataset and accompanying code will be made available, encouraging further exploration and advancement in this field.

7 Acknowledgement

References

[1] Yagiz Aksoy, Changil Kim, Petr Kellnhofer, Sylvain Paris, Mohamed Elgharib, Marc Pollefeys, and Wojciech Matusik. A dataset of flash and ambient illumination pairs from the crowd. In *Proceedings of the European Conference on Computer Vision (ECCV)*, pages 634–649, 2018.

[2] Jonathan T Barron and Jitendra Malik. Shape, illumination, and reflectance from shading. *IEEE transactions on pattern analysis and machine intelligence*, 37(8):1670–1687, 2015.

[3] Sean Bell, Paul Upchurch, Noah Snavely, and Kavita Bala. Opensurfaces: A richly annotated catalog of surface appearance. *ACM Transactions on graphics (TOG)*, 32(4):1–17, 2013.

[4] Sai Bi, Zexiang Xu, Pratul P. Srinivasan, Ben Mildenhall, Kalyan Sunkavalli, Milovs Havsan, Yannick Hold-Geoffroy, David J. Kriegman, and Ravi Ramamoorthi. Neural reflectance fields for appearance acquisition. *ArXiv*, abs/2008.03824, 2020.

[5] Sai Bi, Zexiang Xu, Kalyan Sunkavalli, David Kriegman, and Ravi Ramamoorthi. Deep 3d capture: Geometry and reflectance from sparse multi-view images. In *Proceedings of the IEEE/CVF Conference on Computer Vision and Pattern Recognition*, pages 5960–5969, 2020.

[6] Mark Boss, Raphael Braun, Varun Jampani, Jonathan T Barron, Ce Liu, and Hendrik Lensch. Nerd: Neural reflectance decomposition from image collections. In *Proceedings of the IEEE/CVF International Conference on Computer Vision*, pages 12684–12694, 2021.

[7] Mark Boss, Varun Jampani, Raphael Braun, Ce Liu, Jonathan Barron, and Hendrik Lensch. Neural-pil: Neural pre-integrated lighting for reflectance decomposition. *Advances in Neural Information Processing Systems*, 34:10691–10704, 2021.

[8] Brent Burley and Walt Disney Animation Studios. Physically-based shading at disney. In *ACM SIGGRAPH*, volume 2012, pages 1–7. vol. 2012, 2012.

[9] Anpei Chen, Zexiang Xu, Andreas Geiger, Jingyi Yu, and Hao Su. Tensorf: Tensorial radiance fields. In *Computer Vision–ECCV 2022: 17th European Conference, Tel Aviv, Israel, October 23–27, 2022, Proceedings, Part XXXII*, pages 333–350. Springer, 2022.

[10] Paul Debevec, Tim Hawkins, Chris Tchou, Haarm-Pieter Duiker, Westley Sarokin, and Mark Sagar. Acquiring the reflectance field of a human face. In *Proceedings of the 27th annual conference on Computer graphics and interactive techniques*, pages 145–156, 2000.

[11] Paul Debevec, Andreas Wenger, Chris Tchou, Andrew Gardner, Jamie Waese, and Tim Hawkins. A lighting reproduction approach to live-action compositing. *ACM Transactions on Graphics (TOG)*, 21(3):547–556, 2002.

[12] Yue Dong, Guojun Chen, Pieter Peers, Jiawan Zhang, and Xin Tong. Appearance-from-motion: Recovering spatially varying surface reflectance under unknown lighting. *ACM Transactions on Graphics*, 33(6):193, 2014.

[13] Elmar Eisemann and Frédo Durand. Flash photography enhancement via intrinsic relighting. *ACM transactions on graphics (TOG)*, 23(3):673–678, 2004.

[14] Dan B Goldman, Brian Curless, Aaron Hertzmann, and Steven M Seitz. Shape and spatially-varying brdfs from photometric stereo. *IEEE Transactions on Pattern Analysis and Machine Intelligence*, 32(6):1060–1071, 2009.

[15] Roger Grosse, Micah K Johnson, Edward H Adelson, and William T Freeman. Ground truth dataset and baseline evaluations for intrinsic image algorithms. In *2009 IEEE 12th International Conference on Computer Vision*, pages 2335–2342. IEEE, 2009.

[16] Jon Hasselgren, Nikolai Hofmann, and Jacob Munkberg. Shape, light & material decomposition from images using monte carlo rendering and denoising. *arXiv preprint arXiv:2206.03380*, 2022.

[17] Hideki Hayakawa. Photometric stereo under a light source with arbitrary motion. *JOSA A*, 11(11):3079–3089, 1994.

[18] Carlos Hernandez, George Vogiatzis, and Roberto Cipolla. Multiview photometric stereo. *IEEE Transactions on Pattern Analysis and Machine Intelligence*, 30(3):548–554, 2008.

[19] Rasmus Jensen, Anders Dahl, George Vogiatzis, Engin Tola, and Henrik Aanæs. Large scale multi-view stereopsis evaluation. In *Proceedings of the IEEE conference on computer vision and pattern recognition*, pages 406–413, 2014.

[20] Haian Jin, Isabella Liu, Peijia Xu, Xiaoshuai Zhang, Songfang Han, Sai Bi, Xiaowei Zhou, Zexiang Xu, and Hao Su. Tensoir: Tensorial inverse rendering. In *Proceedings of the IEEE/CVF*

Conference on Computer Vision and Pattern Recognition, pages 165–174, 2023.

[21] Dongyoung Kim, Jinwoo Kim, Seonghyeon Nam, Dongwoo Lee, Yeonkyung Lee, Nahyup Kang, Hyong-Euk Lee, ByungIn Yoo, Jae-Joon Han, and Seon Joo Kim. Large scale multi-illuminant (lsmi) dataset for developing white balance algorithm under mixed illumination. In *Proceedings of the IEEE/CVF International Conference on Computer Vision*, pages 2410–2419, 2021.

[22] Alexander Kirillov, Eric Mintun, Nikhila Ravi, Hanzi Mao, Chloe Rolland, Laura Gustafson, Tete Xiao, Spencer Whitehead, Alexander C Berg, Wan-Yen Lo, et al. Segment anything. *arXiv preprint arXiv:2304.02643*, 2023.

[23] Zhengfei Kuang, Kyle Olszewski, Menglei Chai, Zeng Huang, Panos Achlioptas, and Sergey Tulyakov. Neroic: Neural rendering of objects from online image collections. *ACM Transactions on Graphics (TOG)*, 41(4):1–12, 2022.

[24] Zhengfei Kuang, Yunzhi Zhang, Hong-Xing Yu, Samir Agarwala, Shangzhe Wu, and Jiajun Wu. Stanford-orb: A real-world 3d object inverse rendering benchmark. *arXiv preprint arXiv:2310.16044*, 2023.

[25] Jean-François Lalonde and Iain Matthews. Lighting estimation in outdoor image collections. In *2014 2nd international conference on 3D vision*, volume 1, pages 131–138. IEEE, 2014.

[26] Jason Lawrence, Szymon Rusinkiewicz, and Ravi Ramamoorthi. Efficient brdf importance sampling using a factored representation. *ACM Transactions on Graphics (ToG)*, 23(3):496–505, 2004.

[27] Min Li, Zhenglong Zhou, Zhe Wu, Boxin Shi, Changyu Diao, and Ping Tan. Multi-view photometric stereo: A robust solution and benchmark dataset for spatially varying isotropic materials. *IEEE Transactions on Image Processing*, 29:4159–4173, 2020.

[28] Zhengqin Li, Zexiang Xu, Ravi Ramamoorthi, Kalyan Sunkavalli, and Manmohan Chandraker. Learning to reconstruct shape and spatially-varying reflectance from a single image. In *SIGGRAPH Asia 2018*, page 269. ACM, 2018.

[29] Shanchuan Lin, Andrey Ryabtsev, Soumyadip Sengupta, Brian L Curless, Steven M Seitz, and Ira Kemelmacher-Shlizerman. Real-time high-resolution background matting. In *Proceedings of the IEEE/CVF Conference on Computer Vision and Pattern Recognition*, pages 8762–8771, 2021.

[30] Wan-Chun Ma, Tim Hawkins, Pieter Peers, Charles-Felix Chabert, Malte Weiss, Paul E Debevec, et al. Rapid acquisition of specular and diffuse normal maps from polarized spherical gradient illumination. *Rendering Techniques*, 2007(9):10, 2007.

[31] Ben Mildenhall, Pratul P Srinivasan, Matthew Tancik, Jonathan T Barron, Ravi Ramamoorthi, and Ren Ng. Nerf: Representing scenes as neural radiance fields for view synthesis. *Communications of the ACM*, 65(1):99–106, 2021.

[32] Thomas Müller, Alex Evans, Christoph Schied, and Alexander Keller. Instant neural graphics primitives with a multiresolution hash encoding. *ACM Transactions on Graphics (ToG)*, 41(4):1–15, 2022.

[33] Jacob Munkberg, Jon Hasselgren, Tianchang Shen, Jun Gao, Wenzheng Chen, Alex Evans, Thomas Mueller, and Sanja Fidler. Extracting Triangular 3D Models, Materials, and Lighting From Images. *arXiv:2111.12503*, 2021.

[34] Lukas Murmann, Michael Gharbi, Miika Aittala, and Fredo Durand. A dataset of multi-illumination images in the wild. In *Proceedings of the IEEE/CVF International Conference on Computer Vision*, pages 4080–4089, 2019.

[35] Giljoo Nam, Joo Ho Lee, Diego Gutierrez, and Min H Kim. Practical SVBRDF acquisition of 3D objects with unstructured flash photography. In *SIGGRAPH Asia 2018*, page 267. ACM, 2018.

[36] Georg Petschnigg, Richard Szeliski, Maneesh Agrawala, Michael Cohen, Hugues Hoppe, and Kentaro Toyama. Digital photography with flash and no-flash image pairs. *ACM transactions on graphics (TOG)*, 23(3):664–672, 2004.

[37] Viktor Rudnev, Mohamed Elgharib, William Smith, Lingjie Liu, Vladislav Golyanik, and Christian Theobalt. Nerf for outdoor scene relighting. In *European Conference on Computer Vision (ECCV)*, 2022.

[38] Johannes L Schönberger, Enliang Zheng, Jan-Michael Frahm, and Marc Pollefeys. Pixelwise view selection for unstructured multi-view stereo. In *Computer Vision–ECCV 2016: 14th European Conference, Amsterdam, The Netherlands, October 11-14, 2016, Proceedings, Part III 14*, pages 501–518. Springer, 2016.

[39] Tianchang Shen, Jun Gao, Kangxue Yin, Ming-Yu Liu, and Sanja Fidler. Deep marching tetrahedra: a hybrid representation for high-resolution 3d shape synthesis. In *Advances in Neural Information Processing Systems (NeurIPS)*, 2021.

[40] Boxin Shi, Zhe Wu, Zhipeng Mo, Dinglong Duan, Sai-Kit Yeung, and Ping Tan. A benchmark dataset and evaluation for non-lambertian and uncalibrated photometric stereo. In *Proceedings of the IEEE Conference on Computer Vision and Pattern Recognition*, pages 3707–3716, 2016.

[41] Jessi Stumpfel, Andrew Jones, Andreas Wenger, Chris Tchou, Tim Hawkins, and Paul Debevec. Direct hdr capture of the sun and sky. In *ACM SIGGRAPH 2006 Courses*, pages 5–es. 2006.

[42] Kalyan Sunkavalli, Fabiano Romeiro, Wojciech Matusik, Todd Zickler, and Hanspeter Pfister. What do color changes reveal about an outdoor scene? In *2008 IEEE Conference on Computer Vision and Pattern Recognition*, pages 1–8. IEEE, 2008.

[43] Ariel Tankus and Nahum Kiryati. Photometric stereo under perspective projection. In *Tenth IEEE International Conference on Computer Vision (ICCV'05) Volume 1*, volume 1, pages 611–616. IEEE, 2005.

[44] Marco Toschi, Riccardo De Matteo, Riccardo Spezialetti, Daniele De Gregorio, Luigi Di Stefano, and Samuele Salti. Relight my nerf: A dataset for novel view synthesis and relighting of real world objects. In *Proceedings of the IEEE/CVF Conference on Computer Vision and Pattern Recognition*, pages 20762–20772, 2023.

[45] Jiaping Wang, Peiran Ren, Minmin Gong, John Snyder, and Baining Guo. All-frequency rendering of dynamic, spatially-varying reflectance. In *ACM SIGGRAPH Asia 2009 papers*, pages 1–10. 2009.

[46] Peng Wang, Lingjie Liu, Yuan Liu, Christian Theobalt, Taku Komura, and Wenping Wang. Neus: Learning neural implicit surfaces by volume rendering for multi-view reconstruction. *arXiv preprint arXiv:2106.10689*, 2021.

[47] Yair Weiss. Deriving intrinsic images from image sequences. In *Proceedings Eighth IEEE International Conference on Computer Vision. ICCV 2001*, volume 2, pages 68–75. IEEE, 2001.

[48] Rui Xia, Yue Dong, Pieter Peers, and Xin Tong. Recovering shape and spatially-varying surface reflectance under unknown illumination. *ACM Transactions on Graphics*, 35(6):187, 2016.

[49] Xianmin Xu, Yuxin Lin, Haoyang Zhou, Chong Zeng, Yaxin Yu, Kun Zhou, and Hongzhi Wu. A unified spatial-angular structured light for single-view acquisition of shape and reflectance. In *Proceedings of the IEEE/CVF Conference on Computer Vision and Pattern Recognition*, pages 206–215, 2023.

[50] Lior Yariv, Yoni Kasten, Dror Moran, Meirav Galun, Matan Atzmon, Basri Ronen, and Yaron Lipman. Multiview neural surface reconstruction by disentangling geometry and appearance. *Advances in Neural Information Processing Systems*, 33:2492–2502, 2020.

[51] Kai Zhang, Fujun Luan, Zhengqi Li, and Noah Snavely. Iron: Inverse rendering by optimizing neural sdfs and materials from photometric images. In *Proceedings of the IEEE/CVF Conference on Computer Vision and Pattern Recognition*, pages 5565–5574, 2022.

[52] Kai Zhang, Fujun Luan, Qianqian Wang, Kavita Bala, and Noah Snavely. Physg: Inverse rendering with spherical gaussians for physics-based material editing and relighting. In *Proceedings of the IEEE/CVF Conference on Computer Vision and Pattern Recognition*, pages 5453–5462, 2021.

[53] Xiuming Zhang, Pratul P Srinivasan, Boyang Deng, Paul Debevec, William T Freeman, and Jonathan T Barron. Nerfactor: Neural factorization of shape and reflectance under an unknown illumination. *ACM Transactions on Graphics (TOG)*, 40(6):1–18, 2021.

[54] Yuanqing Zhang, Jiaming Sun, Xingyi He, Huan Fu, Rongfei Jia, and Xiaowei Zhou. Modeling indirect illumination for inverse rendering. In *Proceedings of the IEEE/CVF Conference on Computer Vision and Pattern Recognition*, pages 18643–18652, 2022.

[55] Yuanqing Zhang, Jiaming Sun, Xingyi He, Huan Fu, Rongfei Jia, and Xiaowei Zhou. Modeling indirect illumination for inverse rendering. In *Proceedings of the IEEE/CVF Conference on Computer Vision and Pattern Recognition*, pages 18643–18652, 2022.

[56] Zhenglong Zhou, Zhe Wu, and Ping Tan. Multi-view photometric stereo with spatially varying isotropic materials. In *Proceedings of the IEEE Conference on Computer Vision and Pattern Recognition*, pages 1482–1489, 2013.

Supplementary Material for "OpenIllumination: A Multi-Illumination Dataset for Inverse Rendering Evaluation on Real Objects"

1 Dataset access

URL and data cards. The dataset can be viewed at https://oppo-us-research.github.io/OpenIllumination and downloaded from https://huggingface.co/datasets/OpenIllumination/OpenIllumination.

Author statement. We bear all responsibility in case of violation of rights. We confirm the CC BY (Attribution) 4.0 license for this dataset.

Hosting, licensing, and maintenance plan. We host the dataset on HuggingFace [2], and we confirm that we will provide the necessary maintenance for this dataset.

DOI. 10.57967/hf/1102.

Structured metadata. The metadata is at https://huggingface.co/datasets/OpenIllumination/OpenIllumination.

2 Capturing details

2.1 Object masks

As mentioned in the main paper, our capturing process involves using a device similar to a light stage, which has a diameter of approximately 2 meters. The device consists of cameras and LED lights evenly distributed on the surface of a sphere, all oriented toward the center. To position the object roughly at the center, we utilize two types of supports, as illustrated in Fig. 1(a). However, due to the presence of camera angles that capture views from the bottom to the top, as depicted in Fig. 1(b), certain areas of the surface may be occluded by the supporting device. Consequently, these areas become invisible in these specific views while remaining visible in other views after applying the masking process. This introduces ambiguity to the density field network and leads to inferior performance.

To address this issue and eliminate density ambiguity, we incorporate certain parts of the supporting device in the training images. During the evaluation, we evaluate the PSNR using a separate set of masks that only contain the object. In the dataset, we utilize the *com_mask*, which combines the supporting device and object masks, during the training phase. For inference and evaluation, we employ the *obj_mask*, which represents only the object mask.

2.2 Light pattern design

In addition to the One-Light-At-Time (OLAT) pattern, we have carefully designed 13 different light patterns for our dataset. These patterns involve lighting multiple LED lights either randomly or in a regular manner.

Preprint. Under review.
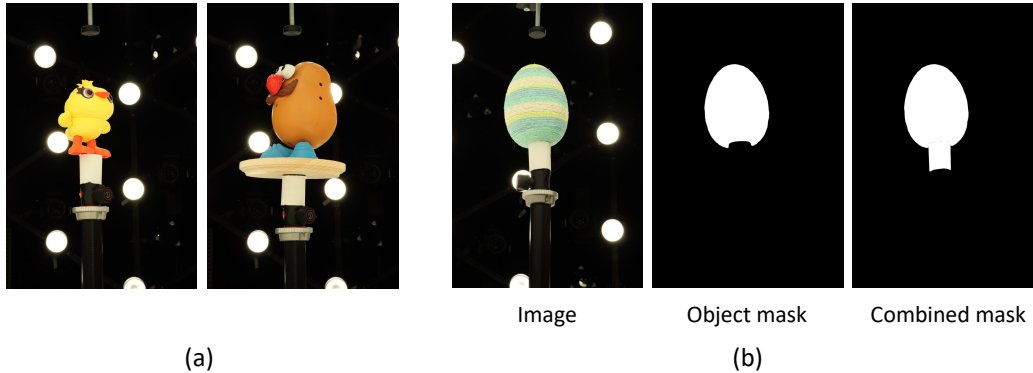
Figure 1: **(a)** Two types of supporting devices used in our dataset. **(b)** We use the combined masks for training to eliminate density ambiguity.

For the first 6 light patterns (001 to 006), we divide the 142 lights into 6 groups based on their spatial location. Each light pattern corresponds to activating one of these groups.

As for the remaining 7 light patterns (007 to 013), the lights are randomly illuminated, with the total number of chosen lights gradually increasing.

Fig. 2 illustrates the 13 light patterns present in our dataset.
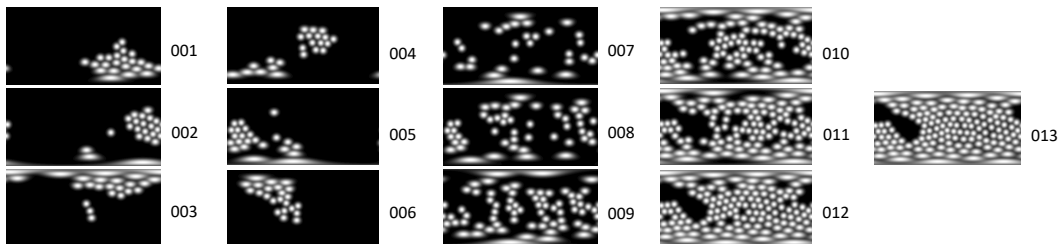
Figure 2: 13 kinds of light patterns in our dataset, shown as an environment map.

2.3 Chrome Ball

In order to perform light calibration, we need to determine the radius and center of the chrome ball in the world coordinate system. This information is crucial for calculating the surface normals at each point on the ball's surface. To ensure accurate intersection point computation, it is important to obtain the radius and position of the chrome ball on the same scale as the camera poses.

To achieve this, we propose using NeuS [3] to extract a mesh with a scale matching the camera poses. We provide multi-view images of the mirror ball as input to NeuS. However, since the mirror ball is highly reflective and difficult to reconstruct accurately using NeuS, we fill the foreground pixels of the mirror ball with black.

Finally, we fit a sphere to the extracted mesh to determine the location and radius of the mirror ball, which allows us to obtain the necessary information for light calibration.

2.4 Camera parameters

During capturing, we set the camera ISO to 100, aperture to F16, and shutter speed to 1/5. We use Daylight mode for its white balance.

We did not perform extra color calibration for the same type of cameras. While it's acknowledged that certain inherent camera intrinsic differences and uncontrollable variables may result in occasional

Figure 3: **Example images of the cylinder.**

color differences, we can observe that the potential differences are very small and negligible from the images and the experimental results.

To further quantify the differences between different cameras, we designed a small experiment. We captured a 3D-printed cylinder, covered with a type of diffuse green paper. The visualization is in Fig. 3. The basic idea is to compute the difference in object surface colors across different cameras. This calculation serves as a rough measurement of the intrinsic differences among different cameras.

To reduce the impact of specular reflections, we use polarizers on the camera systems. In addition, we selected adjacent cameras to reduce the influence of view-dependent color variations. Our findings indicate that the differences between different cameras amount to approximately 1%.

As a result, we can observe that cameras of the same type after setting the same camera parameters already exhibit a high level of consistency without supplementary post-processing calibration procedures.

3   More details of evaluation results

3.1   Code to reproduce the results in the paper

We use the open-source code repositories for the baselines in the paper.

- **NeRD**: https://github.com/cgtuebingen/NeRD-Neural-Reflectance-Decomposition
- **Neural-PIL**: https://github.com/cgtuebingen/Neural-PIL
- **PhySG**: https://github.com/Kai-46/PhySG
- **InvRender**: https://github.com/zju3dv/InvRender
- **Nvdiffrec-mc**: https://github.com/NVlabs/nvdiffrecmc
- **TensoIR**: https://github.com/Haian-Jin/TensoIR
- **NeRF**: https://github.com/KAIR-BAIR/nerfacc
- **TensoRF**: https://github.com/apchenstu/TensoRF
- **instant-NGP**: https://github.com/bennyguo/instant-nsr-pl
- **NeuS**: https://github.com/bennyguo/instant-nsr-pl

3.2 Computational resources

We use a single GTX 2080 GPU for each object to run the baseline experiments.

3.3 Relighting evaluation

We conducted an evaluation of all 64 objects in our dataset using TensoIR [1], which is one of the most recent state-of-the-art (SOTA) inverse rendering methods capable of multi-illumination optimization. For each object, we evaluated the performance of TensoIR under single illumination, multi-illumination, and relighting using novel illuminations. The evaluation results can be found in Tab. 1. Additionally, we include visualizations of the results for a selected number of objects in Fig. 4. As mentioned in the main paper, our dataset provides ground-truth information for the 142 linear polarized LED lights. This allows for the quantitative evaluation of the relighting quality. However, comparing the relighting results directly with the captures without aligning the albedo or light intensity between the two is impractical due to the ambiguity between them in the rendering equation. In practice, we train TensoIR under three different light patterns given their corresponding ground-truth illumination. During the evaluation, we used a different set of ground-truth illumination, along with the learned object's geometry and BRDF, to relight the object. We then compared the relit images with the captures under the new illumination to obtain our relighting evaluation metrics.

Tab. 1 presents the quantitative results of TensoIR's relighting performance on all 64 objects with various materials in our dataset. We used light patterns *009*, *011*, and *013* for training, and the remaining light patterns for evaluation.

References

[1] Haian Jin, Isabella Liu, Peijia Xu, Xiaoshuai Zhang, Songfang Han, Sai Bi, Xiaowei Zhou, Zexiang Xu, and Hao Su. Tensoir: Tensorial inverse rendering. In *Proceedings of the IEEE/CVF Conference on Computer Vision and Pattern Recognition*, pages 165–174, 2023.

[2] Angelina McMillan-Major, Salomey Osei, Juan Diego Rodriguez, Pawan Sasanka Ammana-manchi, Sebastian Gehrmann, and Yacine Jernite. Reusable templates and guides for documenting datasets and models for natural language processing and generation: A case study of the hug-gingface and gem data and model cards. *arXiv preprint arXiv:2108.07374*, 2021.

[3] Peng Wang, Lingjie Liu, Yuan Liu, Christian Theobalt, Taku Komura, and Wenping Wang. Neus: Learning neural implicit surfaces by volume rendering for multi-view reconstruction. *arXiv preprint arXiv:2106.10689*, 2021.

Object ID	Material	Single Illum	Multi-Illum	Relighting	Object ID	Material	Single Illum	Multi-Illum	Relighting
1	plastic	24.43	24.70	26.41	33	fabric	29.30	28.97	28.00
2	paper	34.13	34.48	31.99	34	wax	43.36	42.39	34.29
3	plastic	36.21	35.84	33.01	35	clear-plastic	22.53	22.58	22.96
4	stone	31.15	30.07	31.07	36	sponge	32.49	32.18	30.86
5	painted	30.53	30.80	30.16	37	fabric	30.98	30.58	28.70
6	ceramic	35.49	35.40	33.07	38	foliage	25.53	25.03	26.89
7	fabric	32.64	31.87	29.65	39	plastic	34.04	33.67	31.46
8	clear-plastic	23.12	23.43	26.41	40	plant	27.74	27.61	30.26
9	paper	33.98	33.53	31.21	41	fabric	34.12	33.66	29.51
10	paper, plastic	30.15	29.92	28.66	42	food	35.18	34.69	32.13
11	plastic	34.19	33.81	29.95	43	paper	42.16	41.26	31.29
12	leather	28.89	28.45	29.47	44	fabric	32.78	32.38	29.45
13	ceramic	32.04	32.16	29.95	45	metal	28.22	28.08	29.62
14	metal, plastic	27.82	28.12	29.31	46	fabric	29.02	28.59	29.58
15	fabric, plastic	28.99	28.78	28.71	47	painted	32.16	31.71	33.62
16	plastic	35.02	34.70	32.84	48	metal	29.09	29.57	27.13
17	coated	26.18	26.52	27.57	49	rubbery	27.51	27.22	28.69
18	glass	29.61	29.54	27.68	50	fabric	31.31	30.55	28.66
19	ceramic	31.56	31.22	29.55	51	plastic	30.47	29.90	30.56
20	ceramic	29.31	29.31	28.63	52	hair	22.65	22.50	22.51
21	paper	35.94	35.39	29.85	53	rubbery	30.21	30.77	28.32
22	wooden	19.72	20.30	23.00	54	leather	29.60	29.34	29.84
23	paper	36.18	35.46	30.82	55	stone	36.33	35.79	31.99
24	latex	26.22	26.04	27.32	56	fabric	30.21	30.12	29.03
25	latex	28.93	28.67	27.93	57	cloth	30.05	29.77	24.70
26	wicker	28.97	28.26	27.16	58	wicker	28.76	28.45	28.77
27	foam	34.03	33.36	30.70	59	nylon	34.70	34.52	32.75
28	metal	28.82	28.57	30.82	60	fabric	36.66	36.13	33.61
29	fabric	32.30	31.83	32.38	61	fabric	29.93	29.51	29.35
30	foam	30.20	29.97	29.97	62	fabric	36.56	35.90	31.85
31	painted	30.66	30.58	30.00	63	fabric	35.63	35.53	31.95
32	stone	31.82	31.53	29.75	64	paper	31.24	30.01	27.62

Table 1: **Evaluation results of TensoIR on all objects in our dataset**. We report the PSNR values of each object under single illumination, multi-illumination, and their relighting PSNR under novel illuminations.
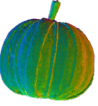
Figure 4: **Material reconstruction and relighting results on a selective number of objects in our dataset.** We show the decomposed albedo, normal, rendering image, and relighting image under novel illumination. In general, objects with diffuse surfaces have better results than objects with specular surfaces. For example, it is difficult to correctly reconstruct normal in highly-specular areas for object No.37.